

Improved estimate of the detectability of gravitational radiation from a magnetically confined mountain on an accreting neutron star

M. Vigelius ^{1*} and A. Melatos ¹

¹ *School of Physics, University of Melbourne, Parkville, VIC 3010, Australia*

Submitted to MNRAS

ABSTRACT

We give an improved estimate of the detectability of gravitational waves from magnetically confined mountains on accreting neutron stars. The improved estimate includes the following effects for the first time: three-dimensional hydromagnetic (“fast”) relaxation, three-dimensional resistive (“slow”) relaxation, realistic accreted masses $M_a \lesssim 2 \times 10^{-3} M_\odot$, (where the mountain is grown ab initio by injection), and verification of the curvature rescaling transformation employed in previous work. Typically, a mountain does not relax appreciably over the lifetime of a low-mass X-ray binary. The ellipticity reaches $\epsilon \approx 2 \times 10^{-5}$ for $M_a = 2 \times 10^{-3} M_\odot$. The gravitational wave spectrum for triaxial equilibria contains an additional line, which, although weak, provides valuable information about the mountain shape. We evaluate the detectability of magnetic mountains with Initial and Advanced LIGO. For a standard, coherent matched filter search, we find a signal-to-noise ratio of $d = 28(M_a/10^{-4} M_\odot)(1 + 5.5M_a/10^{-4} M_\odot)^{-1}(D/10 \text{ kpc})^{-1}(T_0/14 \text{ d})^{1/2}$ for Initial LIGO, where D is the distance and T_0 is the observation time. From the nondetection of gravitational waves from low-mass X-ray binaries to date, and the wave strain limits implied by the spin frequency distribution of these objects (due to gravitational wave braking), we conclude that there are other, as yet unmodelled, physical effects that further reduce the quadrupole moment of a magnetic mountain, most notably sinking into the crust.

Key words: accretion, accretion disks – stars: magnetic fields – stars: neutron – pulsars: general

1 INTRODUCTION

Accreting neutron stars in low-mass X-ray binaries (LMXBs) are promising sources of continuous gravitational waves (GWs). The signal from these emitters can be coherently integrated, so that the signal-to-noise ratio increases with the square root of the observation time (Jaranowski et al. 1998). Recent directed searches for GWs from the nearby X-ray source Sco X–1 by the Laser Interferometer Gravitational Wave Observatory (LIGO) set an upper bound on the gravitational wave strain of $h_0 \lesssim 10^{-22}$ (Abbott et al. 2007).

LMXBs emit continuous gravitational waves via a variety of physical mechanisms (Owen 2006; Abbott et al. 2007): nonaxisymmetric elastic deformations of the neutron star crust, generated by temperature gradients (Bildsten 1998; Ushomirsky et al. 2000; Haskell et al. 2007) or inter-

nal toroidal magnetic fields (Cutler 2002); r-modes, generated by the Chandrasekhar-Friedmann-Schutz instability (Owen et al. 1998; Andersson et al. 1999; Stergioulas 2003; Nayyar & Owen 2006); free precession, excited by internal or accretion torques (Jones & Andersson 2002; Van Den Broeck 2005; Payne & Melatos 2006a; Chung et al. 2008); and magnetically confined mountains (Payne & Melatos 2004; Melatos & Payne 2005; Payne & Melatos 2006a; Vigelius & Melatos 2008a,b).

In the latter mechanism, accreting plasma accumulates at the magnetic poles and spreads equatorwards. The frozen-in magnetic field is carried along with the spreading plasma and is therefore compressed, to the point where magnetic tension counterbalances the latitudinal pressure gradient. This equilibrium configuration is termed a magnetic mountain (Payne & Melatos 2004). During the process, the magnetic dipole moment of the star decreases with accreted mass, consistent with observational data (Zhang 1998; Melatos & Phinney 2001; Payne & Melatos 2004;

* E-mail: mvigeliu@physics.unimelb.edu.au

Zhang & Kojima 2006). The distorted magnetic field can also act as a thermal barrier between the hemispheres, affecting the physics of type I X-ray bursts (Payne & Melatos 2006b).

In this paper, we draw together the latest analytic and numerical modelling of magnetic mountains in LMXBs (Vigelius & Melatos 2008a,b) to compute rigorously the signal-to-noise ratio of these sources for a coherent search with LIGO. To this end, we make extensive use of previously published results. Hydromagnetic equilibria of magnetically confined mountains were computed analytically and numerically by Payne & Melatos (2004). While these configurations are stable to axisymmetric perturbations (Payne & Melatos 2007), the (nonaxisymmetric) undulating submode of the three-dimensional Parker instability induces a reconfiguration of the magnetic field (Vigelius & Melatos 2008a). However, the line-tying boundary condition at the stellar surface prevents the mountain from being disrupted and the saturation state of the instability still exhibits a substantial quadrupole moment with a high degree of axisymmetry. Vigelius & Melatos (2008b) extend the analysis to include resistive effects and demonstrate that the mountain decays on the diffusion time scale. No evidence for resistive instabilities that grow on a short time scale is found.

In their stability analysis, Payne & Melatos (2006a) and Vigelius & Melatos (2008a,b) numerically computed an equilibrium configuration with a particular value for the accreted mass, M_a , subsequently loaded this equilibrium into a magnetohydrodynamic (MHD) solver and evolved it. In this article, we solve the initial-value MHD problem for the first time by injecting plasma into an initially dipolar field. This method allows us to independently validate and extend the scalings given by Payne & Melatos (2004) and Melatos & Payne (2005), which were calculated analytically in the small- M_a approximation. Taking into account resistive effects and three-dimensional reconfiguration of the mountain, we present easily applicable formulas to compute the mass ellipticity for a given M_a and give improved estimates on the strength of the gravitational wave emission. In particular, we investigate how the (small) degree of non-axisymmetry changes the gravitational wave spectrum and how gravitational-wave spectrometry can be used to obtain valuable information about the underlying field configuration. This analysis ties in with Payne & Melatos (2006a) who consider axisymmetric mountains.

The paper is organised as follows. We describe quantitatively the physics of the mass quadrupole moment of a magnetic mountain in section 2, including three-dimensional force balance, slow (resistive) and fast (hydromagnetic) relaxation, realistic accreted masses, and the influence of stellar curvature. Taking into account these effects, we give a recipe to compute the quadrupole moment as a function of accreted M_a in section 3 and hence estimate the strength and detectability of the GW signal. The frequency spectrum of the signal is calculated in section 4. We discuss our results in the context of past and future LIGO searches in section 5.

2 MASS QUADRUPOLE MOMENT OF A MAGNETIC MOUNTAIN

In the context of gravitational radiation, the key property of a magnetic mountain is its mass quadrupole moment,

$$Q_{ij} = \int d^3\mathbf{x}' (3x'_i x'_j - r'^2 \delta_{ij}) \rho(\mathbf{x}'), \quad (1)$$

where ρ denotes the plasma density. We aim to calculate Q_{ij} as a function of the accreted mass M_a . It is useful to measure M_a in units of the critical mass $M_c = GM_* B_*^2 R_*^2 / (8c_s^4)$, where M_* and R_* are the stellar mass and radius, $B_* = 10^{12}$ G is the initial magnetic field, and $c_s = 10^8$ cm s⁻¹ is the isothermal sound speed. For $M_a > M_c$, the magnetic dipole moment μ decreases with M_a ; for $M_a < M_c$, μ is approximately constant (Payne & Melatos 2004). In a typical LMXB, we have $10^{-5} \lesssim M_c/M_\odot \lesssim 10^{-4}$ and $10^{-2} \lesssim M_a/M_\odot \lesssim 10^{-1}$; that is, magnetic burial distorts the field dramatically.

The three-dimensional equilibria computed by Vigelius & Melatos (2008a) deviate from axisymmetry (with respect to the *magnetic* axis) by less than 0.1 per cent in the mass quadrupole moment. Hence, we frequently employ the axisymmetric mass ellipticity, defined as

$$\epsilon = \frac{\pi}{I_{zz}} \int d\theta dr \rho r^4 \sin\theta (3\cos^2\theta - 1), \quad (2)$$

to describe the mountain as a biaxial ellipsoid, where $I_{zz} = 2M_* R_*^2 / 5$ denotes the unperturbed moment of inertia.

In order to give a reliable estimate of the magnitude of ϵ and hence the strength of the gravitational wave signal, we take into account the effects of hydromagnetic (Vigelius & Melatos 2008a) and resistive (Vigelius & Melatos 2008b) relaxation and consider the high- M_a limit as well as the influence of the neutron star curvature. For the convenience of the reader, we repeat previously published results in the first three subsections. We compute Q_{ij} for the three-dimensional equilibrium state in section 2.1. We then examine how the mountain responds to hydromagnetic and resistive relaxation in sections 2.2 and 2.3 respectively. Section 2.4 explains how to build mountains with realistic values of M_a , and the effect of curvature downscaling is quantified in section 2.5. The results in the last two subsections are new and have not been published elsewhere.

2.1 Three-dimensional equilibrium

In a magnetic mountain at equilibrium, the pressure gradient balances the gravitational and Lorentz forces. Starting with a centred magnetic dipole before accretion begins, Payne & Melatos (2004) computed the unique, self-consistent, Grad-Shafranov equilibrium that satisfies force balance, while simultaneously respecting the flux-freezing constraint of ideal magnetohydrodynamics (MHD).

The top-left panel of Fig. 1 displays an axisymmetric equilibrium for $M_a = M_c$. The mountain (orange isosurface) is confined to the magnetic pole by the tension of the distorted magnetic field (blue and green curves). Blue and green field lines are drawn starting from the pole and equator, respectively. The region where the magnetic pressure is greatest (at $\theta \approx \pi/4$ in Fig. 1a) is termed the equatorial

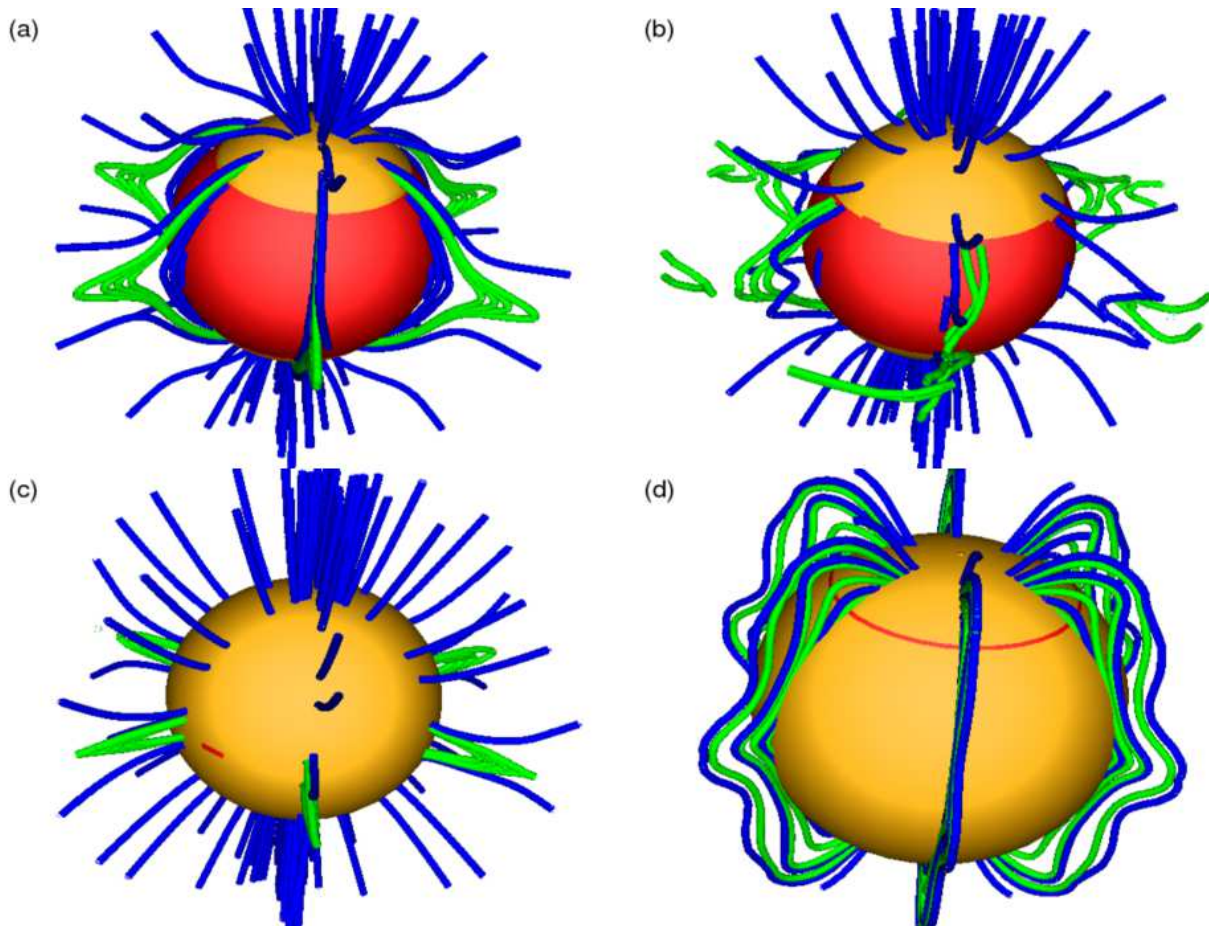


Figure 1. Density isosurface (orange) and magnetic field lines (blue and green) for a magnetic mountain. (a) Axisymmetric, ideal-MHD configuration with $M_a = 1.2 \times 10^{-4} M_\odot$. (b) Nonaxisymmetric, ideal-MHD configuration with $M_a = 1.2 \times 10^{-4} M_\odot$. (c) Snapshot of the resistive evolution at $t = 10\tau_A$, with $M_a = 1.2 \times 10^{-4} M_\odot$. (d) A mountain grown by injection with $M_a = 1.9 \times 10^{-3} M_\odot$. The mountain is defined by the orange isosurface $\rho(r, \theta, \phi) = 0.5\rho_{\max}$, where $\rho_{\max} = 2.0 \times 10^9 \text{ g cm}^{-3}$ is reached at $\hat{x} = (r - R_*)/h_0 = 0.9 \times 10^{-3}$ and $\theta = 0.01$ in the axisymmetric model. In order to aid the reader, the altitude scales are magnified five-fold in all panels. The foot points of the blue field lines touch the stellar surface, while green field lines are traced starting from the equator.

magnetic belt. Here, B is ~ 16 times higher than at the pole.

However, an axisymmetric analysis neglects important toroidal modes. When we load the axisymmetric equilibrium in Fig. 1a into the ideal-MHD code ZEUS-MP, we observe that it is unstable to the undulating submode of the three-dimensional Parker instability, which reconfigures the hydromagnetic structure by growing the toroidal magnetic field (Vigelius & Melatos 2008a). Thanks to line tying, the instability is not disruptive; its saturation state (Fig. 1b) still confines matter at the magnetic pole, and the mountain is still present even though ϵ is reduced to ~ 60 per cent of its original value. The evolution of Q_{ij} for this model (Fig. 1b) is displayed in Fig. 2. The diagonal components, describing the axisymmetric distortions, decrease by ≈ 40 per cent, on a time-scale of $\approx 2\tau_A$. Here, $\tau_A = (\pi R_* \rho^{1/2}/B)_{\min}$ denotes the pole-equator crossing time for transverse Alfvén waves; $\pi R_* \rho^{1/2}/B$ is smallest close to the stellar surface. For a realistic star with $M_a = M_c$, the Alfvén time-scale evaluates to $\tau_A = 5.1 \times 10^{-2} \text{ s}$.

2.2 Fast, hydromagnetic relaxation

A magnetic mountain performs global hydromagnetic oscillations when perturbed, but it remains intact. This unexpected outcome can be ascribed to two factors: (i) the mountain is already the saturation state of the nonlinear Parker instability, and (ii) the line-tying at the stellar surface suppresses important localised modes, e.g. interchange modes. Payne & Melatos (2007) found all mountains with $M_a \leq 6 \times 10^{-4} M_\odot$ to be marginally stable.

The mountain quickly tends to an almost axisymmetric state ($|Q_{12}/Q_{33}| < 10^{-3}$ in Fig. 2). This high degree of axisymmetry considerably simplifies the computation of the amplitude of the gravitational wave strain (see section 3.1). (Note that Q_{ij} is defined relative to the magnetic axis, which is inclined with respect to the rotation axis). The reconfiguration is accompanied by global, nonaxisymmetric, MHD oscillations (top panel of Fig. 2). Although they die away in this numerical experiment, global oscillations can be continuously excited in reality (e.g. by accretion torques), modifying the gravitational wave spectrum (see section 4). Payne & Melatos (2007) identified two dominant modes: a short-period sound mode, with a frequency

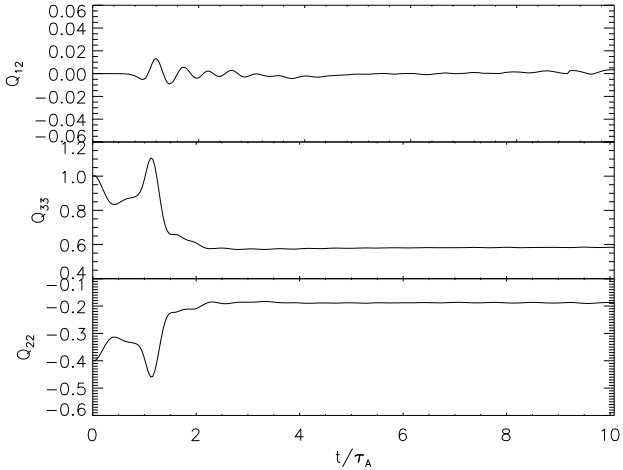


Figure 2. Quadrupole moments for the nonaxisymmetric configuration (Fig. 1b), normalised to $Q_{33} = 1.30 \times 10^{25} \text{ g cm}^2$ of the axisymmetric model, as a function of time, in units of the Alfvén time, $\tau_A = 5.1 \times 10^{-2} \text{ s}$. The system develops an appreciable nonaxisymmetry, characterised by the off-diagonal element Q_{12} , during the relaxation phase before settling into a nearly axisymmetric state.

$f_S/\text{kHz} = 1.4 \times 10^5 (c_s/10^8 \text{ cm s}^{-1})$ (independent of M_a), and a longer period Alfvén oscillation, which can be fitted by $f_A = 17(M_a/M_c) \text{ Hz}$.

(Litwin et al. 2001) demonstrated that an accretion column that is magnetically confined to the polar cap is susceptible to the ideal-MHD ballooning instability. However, our simulations do not exhibit any evidence for a growing instability. Physically, this is because the compressed equatorial magnetic field stabilises the lateral motions involved in such an instability. Indeed, in Fig. 3, we demonstrate that a magnetically confined mountain is only susceptible to a growing ballooning mode when the back-reaction of the magnetic belt is neglected. We perform an axisymmetric simulation with $M_a = M_c$ and $0 \leq \theta \leq \pi/8$, where the outer θ -boundary (at $\theta = \pi/8$) is set to **outflow**. The mountain is clearly disrupted on the Alfvén timescale by the ballooning mode, as in Fig. 3; the magnetic field and frozen-in plasma slide sideways through the outflow boundary. This is consistent with the findings of Litwin et al. (2001), who imposed boundary conditions equivalent to outflow, therefore neglecting the stabilizing effect of the equatorial magnetic belt. Furthermore, our growing simulations do not show any evidence for an instability during the early stages of accretion (when $M_a \ll M_c$).

2.3 Slow, resistive relaxation

A magnetic mountain relaxes resistively over a long time-scale, which is set by the ohmic diffusion rate across the steepest magnetic gradients in the mountain. Resistive relaxation reduces Q_{ij} . Simple estimates suggest that the effect can be neglected as long as $M_a \lesssim 10^{-5} M_\odot$, assuming a homogeneous conductivity, $\sigma = 7.7 \times 10^{26} \text{ s}^{-1}$ (Melatos & Payne 2005). Here, we assume that σ is dominated by electron-phonon scattering, with a crustal temperature $T = 10^7 \text{ K}$ and a characteristic plasma density of $\rho = 5 \times 10^{13} \text{ g cm}^{-3}$ (Cumming et al. 2004). There are

considerable uncertainties about the exact value of σ , such as the value of the impurity parameter (Schatz et al. 1999; Cumming et al. 2001, 2004; Jones 2004; Pons & Geppert 2007) and the composition of the crust (Cumming et al. 2004; Chamel & Haensel 2008). Furthermore, σ is in reality a function of the location through T and ρ . In keeping with Vigelius & Melatos (2008b), we treat the electrical conductivity as a fiducial parameter and note that the time-scale of resistive relaxation scales with σ . An inhomogeneous conductivity will be considered in a forthcoming paper.

Transient resistive instabilities, like a global tearing mode or local gravitational mode (Furth et al. 1963), are known to evolve on time-scales as short as $\sim (\tau_D \tau_A)^{1/2} \approx 0.3 \text{ yr}$, where τ_D denotes the characteristic diffusion time-scale. Note that τ_D implicitly depends on the position through \mathbf{B} and ρ and has a minimum close to the surface. The definition of the characteristic diffusion timescale is hence somewhat arbitrary. As justified in section 2.1, we pick the minimum value $\tau_D = (4\pi\sigma B/c^2 |\nabla^2 \mathbf{B}|)_{\min}^{-1/2}$. Instabilities grow in magnetic neutral sheets [created by the undulating submode of the Parker instability; see Hanasz et al. (2002)] or regions of high magnetic shear.

Vigelius & Melatos (2008b) tested numerically whether neutral sheets can grow to disrupt the mountain on short time-scales. They evolved the three-dimensional equilibrium in Fig. 1b, and similar states for other values of M_a , in ZEUS-MP, extended to treat ohmic diffusion. The results are reported in Fig. 4, which depicts the evolution of ϵ for different Lundquist numbers $Lu = \tau_D/\tau_A$. For each value of Lu , $\epsilon(t)$ is plotted as a function of time, measured in units of the Alfvén time¹ $\tau_A = 2.5 \times 10^{-2} \text{ s}$ (left panel) and the diffusion time τ_D (right panel), which differs for each model. The models with a realistic resistivity ($Lu = 10^{14}$, solid curve) and $Lu = 10^3$ (dotted) do not exhibit any change in ϵ over the simulation time. For $Lu = 10^5$ (dashed), we note a decrease of 21 per cent over $\sim 0.1\tau_D$. For $Lu = 10^{-2}$ (dash-dotted), the mountain relaxes substantially; ϵ drops by 90 per cent over the diffusion time-scale. For $Lu = 10^{-3}$ (dash-triple-dotted), the mountain immediately slips through the magnetic field lines and falls freely towards the equator, where it is reflected by the boundary surface, causing ϵ to oscillate. The latter case, in particular, is of academic interest only, as far as its application in LMXBs is concerned. Magnetic neutral sheets are found in the toroidal plane, where the plasma density and magnetic field strength are low. Reconnection occurs locally in these regions, smoothing toroidal gradients. Ohmic dissipation therefore tends to restore axisymmetry.

Importantly, the mountain relaxes globally on the diffusion time-scale, τ_D , which greatly exceeds the accretion time-scale τ_{acc} , with ϵ falling to e^{-1} of its initial value after $34\tau_D$. In practice, this means that the three-dimensional saturation state of the Parker instability does not relax resistively until $\sim 10^7 \text{ yr}$ elapse, at least for the examined mountains with $M_a \lesssim 10^{-4} M_\odot$. In the analytic small- M_a limit, Melatos & Payne (2005) found the minimum accreted mass for ohmic diffusion to arrest mountain growth to be $M_d \sim 10^{-7} M_\odot$, provided the star accretes at the Eddington

¹ In Fig. 4, τ_A is the characteristic Alfvén time-scale for the three-dimensional equilibrium. It is half the characteristic Alfvén time-scale of the axisymmetric configuration used in section 2.1.

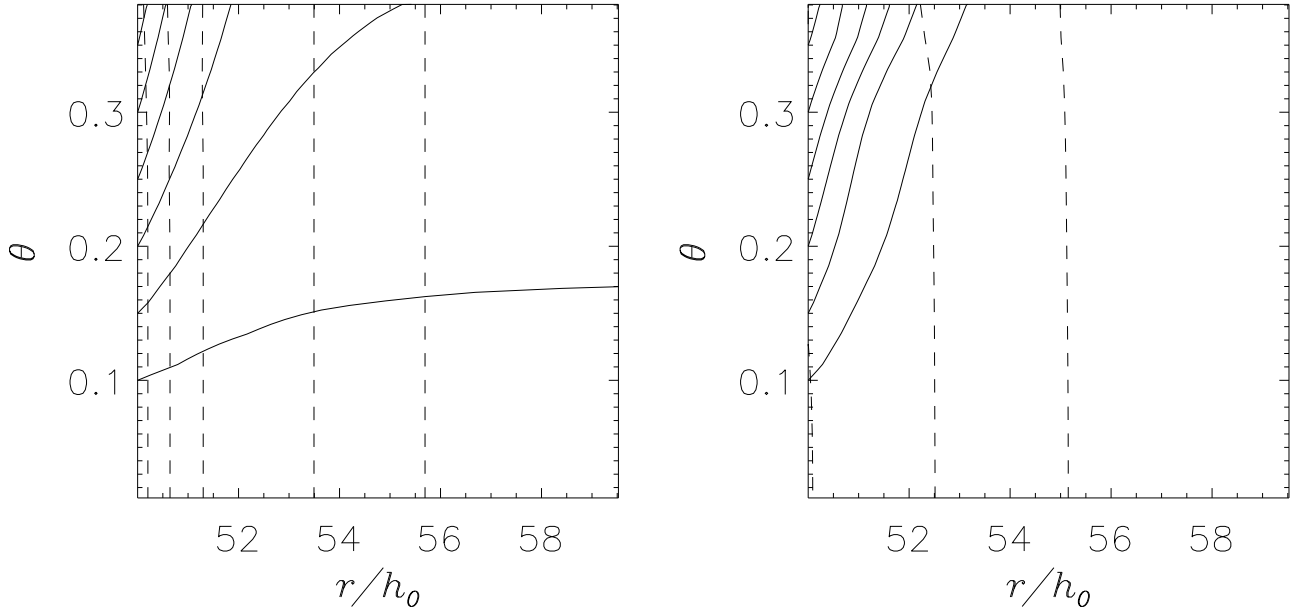


Figure 3. Meridional section of a mountain with $M_a = M_c$ and outflow boundary conditions at $\theta = \pi/8$ at $t = 0$ (left panel) and $t = 0.9\tau_A$ (right panel). The mountain is susceptible to an ideal-MHD ballooning instability and disrupts over the Alfvén timescale.

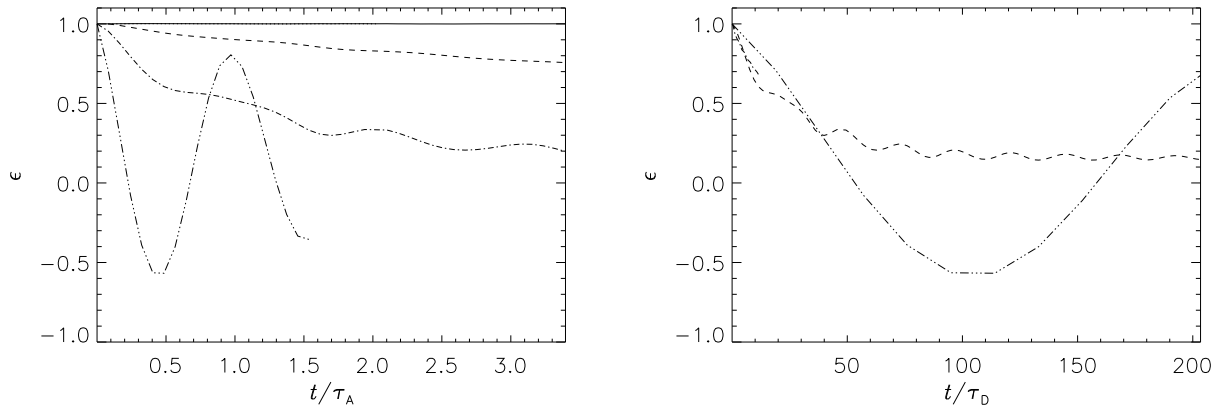


Figure 4. Evolution of mass ellipticity ϵ for different values of the Lundquist number $Lu = \tau_D/\tau_A = 10^{14}, 10^3, 10^{-1}, 10^{-2}, 10^{-3}$ (solid, dotted, dashed, dash-dotted, dash-triple-dotted), curves from top to bottom, in units of the Alfvén time $\tau_A = 2.5 \times 10^{-21}$ s (left panel) and the respective diffusion times τ_D (right panel). The solid and dotted curves nearly overlap. The magnetic mountain relaxes at the time-scale τ_D , with ϵ falling to e^{-1} of its initial value after $34\tau_D$. Two of the curves are hard to see in the right panel: $Lu = 10^{14}$ (solid) stops at $t = \tau_D$ and $Lu = 10^3$ (dotted) stops at $t = 10\tau_D$.

rate (such that $\tau_{\text{acc}} = M_d/\dot{M}_a \sim 10^5$ yr) and has a crustal temperature of $T = 10^8$ K. Our numerical result, independently validated in section 2.4, raises M_d by three orders of magnitude.

In addition to resistive effects in the accreted plasma, Konar & Bhattacharya (1997) explored the influence of ohmic dissipation on the crustal magnetic field. They identified three competing mechanisms: (i) the accretion flow advects current into lower layers with higher ρ and consequently higher σ ; (ii) the crust is heated by advection, decreasing σ ; and (iii) the current is squeezed into the inner

layers, decreasing τ_D . As a result, the crustal field decays rapidly before freezing at a residual surface value, whose magnitude increases with \dot{M}_a [by reducing the duration of the rapid decay phase, see also Romani (1990)]. We defer the study of sinking and stratified σ [compare, e.g., (Jahan-Miri 2000; Choudhuri & Konar 2002)] to future work.

2.4 Realistic accreted mass

Numerical obstacles, like steep gradients, and physical obstacles, like magnetic bubble formation, interfere with the task of modelling magnetic mountains for realistic values of M_a . The iterative numerical scheme employed by Payne & Melatos (2004) to compute Grad-Shafranov equilibria converges poorly for $M_a \gtrsim 10^{-4} M_\odot$. A bootstrapping algorithm can be used to quasistatically fatten a Grad-Shafranov equilibrium ten-fold (Payne & Melatos 2007), but the results have not yet been verified against a reliable numerical solution of the full initial-value problem (bootstrapping converges quite violently), and anyway, bootstrapping works up to $M_a \sim 10^{-3} M_\odot$ at most. In short, a self-consistent configuration with a realistic amount of accreted matter, e.g. $M_a \sim 0.1 M_\odot$ (Burderi et al. 1999), is yet to be achieved.

We try to overcome this restriction in this subsection by growing a magnetic mountain from scratch, by injecting plasma at the inner boundary $r = R_*$ into an initially dipolar background field. The injection speed is chosen to be less than the gravitational escape speed from the simulation box, while the density is chosen to give $\tau_A \ll \tau_{\text{acc}}$, such that the system passes through a sequence of *quasistatic* equilibria, yet τ_{acc} is short enough to keep the simulation runtime reasonable for $M_a \sim 10^{-3} M_\odot$. This approach differs from the bootstrapping algorithm (Payne & Melatos 2007) in two ways: (i) instead of relying on a Grad-Shafranov equilibrium as the starting point, we solve the full initial-value problem; and (ii) we inject plasma at the $r = R_*$ boundary, thereby circumventing the artificial field line pinning at the outer boundary that stems from the *inflow* boundary condition. Implementation details are provided in Appendix A.

An axisymmetric grown mountain with $M_a = 1.9 \times 10^{-3} M_\odot$ and $b = 3$ (hemispheric-polar magnetic flux ratio; see Appendix A) is displayed in panel (d) of Fig. 1. The mountain isosurface covers the whole star. The base density, at $(\tilde{x}, \theta) = (10^{-3}, 0.012)$ is fifty times higher than for $M_a = 1.2 \times 10^{-4} M_\odot$ [panel (a)]. At first glance, the magnetic field configuration looks entirely different: instead of pointing radially outward, all field lines are closed loops. This ostensible difference is due to the boundary condition $\partial \mathbf{B} / \partial r = 0$ at $r = R_m$, enforced in the growing simulations (see Appendix A), cf. $B_\theta = 0$ in Payne & Melatos (2004). However, appearances are a bit misleading: the all-important equatorial belt, where the magnetic field is highly distorted and most intense, is clearly visible in Fig. 1d, just as much as Figs. 1a – 1c. Near the pole, at $(\tilde{x}, \theta) = (10^{-3}, 0.012)$, B in model d is comparable to B in model a. At the magnetic equator, $(\tilde{x}, \theta) = (10^{-3}, 1.4)$, B is ~ 25 times higher in model d than in model a. Naturally, the magnetic tension required to counterbalance the hydrostatic pressure is greater in model d.

Fig. 5 shows the evolution of ϵ as a function of M_a up to $M_a \leq 1.9 \times 10^{-3} M_\odot$. Plotted are models with zero resistivity (solid curve), a realistic resistivity $\eta = 1.3 \times 10^{-27}$ s [Cumming et al. (2004), plus symbols], and an artificially high resistivity, $\eta = 9.2 \times 10^{-13}$ s (i.e. $Lu = \tau_D / \tau_A = 10^5$, dashed curve). We also fit a functional dependence similar to that proposed by Shibazaki et al. (1989) and Melatos & Payne (2005) to the plus symbols, finding

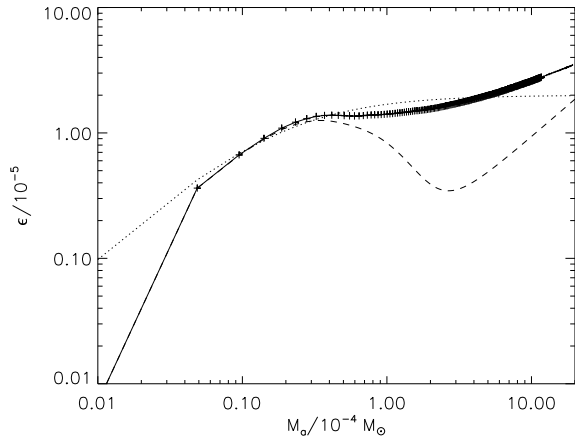


Figure 5. Mass ellipticity ϵ as a function of M_a . The solid curves show a model with zero resistivity (solid curve), realistic resistivity $\eta = 1.3 \times 10^{-27}$ s (plus symbols), and an artificially high resistivity $\eta = 9.2 \times 10^{-13}$ s (dashed curve). The dotted curve represents a fit to the (slightly modified) formula given in Melatos & Payne (2005); see equation (3).

$$\frac{\epsilon}{10^{-5}} = 11 \frac{M_a}{10^{-4} M_\odot} \left(1 + 5.5 \frac{M_a}{10^{-4} M_\odot} \right)^{-1}. \quad (3)$$

The fitting formula is plotted as a dotted curve in Fig. 5.

Fig. 5 and equation (3) are indispensable tools for calculating the gravitational wave emission, summarising as they do our most up-to-date modelling of resistive relaxation and large (i.e. realistic) values of M_a . For $M_a \gtrsim 0.5 \times 10^{-4} M_\odot$, ϵ is expected and found to follow the shape of the small- M_a analytic solution, valid for $M_a \ll M_c = 1.2 \times 10^{-4}$ [see Appendix in Payne & Melatos (2004)]. The deviation visible at $M_a = 10^{-6} M_\odot$ can be attributed to the fact that the configuration has not yet had time to equilibrate. In this regime, material piles up in a polar flux tube of approximately constant cross-sectional area, yielding $\epsilon \propto M_a$. For $M_a \gtrsim 10^{-5} M_\odot$, the hydrostatic pressure overcomes the magnetic tension and the mountain spreads towards the equator, triggering global MHD oscillations. These lateral oscillations, observed numerically by Payne & Melatos (2007), compress the magnetic field once per cycle, increasing $|\nabla^2 \mathbf{B}|$, promoting lateral diffusion of the mountain, and reducing ϵ . For high η (dashed curve), the oscillation in ϵ is clearly visible in Fig. 5. It is also visible, albeit less prominently, for realistic η (plus symbols in Fig. 5). Hence the fairest way to interpret the ϵ - M_a trend in Fig. 5 is that ϵ saturates for $M_a \gg M_c$ (flat underlying trend) with an oscillation superposed.

In a realistic accretion scenario, given \dot{M}_a , we expect to find one particular value of M_a (and hence ϵ) at which the system attains a steady state, where the mass diffuses through flux surfaces at a rate which is exactly replenished by \dot{M}_a . A full parameter study to examine the relation $\epsilon(\dot{M}_a)$ is outside the scope of this article. We simply note, following Vigelius & Melatos (2008b), that magnetic mountains are resistively stable over τ_{acc} or $M_a \leq 1.2 \times 10^{-4} M_\odot$ (neglecting mass inflow).

Can short-timescale instabilities that are absent in the equilibrium configuration grow during the early stages of ac-

cretion, i.e. for small M_a ? In this case, high- M_a equilibria could never be reached and magnetic mountains would not emit detectable gravitational radiation. However, our growing simulations (Fig. 5) show no evidence for ideal-MHD or resistive instabilities during the low- M_a stage of accretion.

2.5 Realistic curvature

In general, the characteristic length-scale for radial gradients (h_0) is much smaller than the length-scale for latitudinal gradients (R_*), creating numerical difficulties. However, in the small- M_a limit, it can be shown analytically (Payne & Melatos 2004, 2006a) that the structure of the magnetic mountain depends on R_* and M_* through the combination $h_0 \propto R_*^2/M_*$, not separately. We therefore artificially reduce R_* and M_* , while keeping h_0 fixed, to render the problem tractable computationally. It is vital to bear in mind that invariance of the equilibrium structure under this curvature rescaling does not imply invariance of the dynamical behaviour, nor is the scaling necessarily applicable at large M_a .

A standard neutron star has $M_* = 1.4M_\odot$, $R_* = 10^6$ cm, $B_* = 10^{12}$ G, and $c_s = 10^8$ cm s $^{-1}$. We rescale the star to $M'_* = 1.0 \times 10^{-5}M_\odot$ and $R'_* = 2.7 \times 10^3$ cm, reducing $a = R_*/h_0$ to 50 while keeping it large. We then calculate the mountain structure, and hence ϵ numerically. We upscale M_a back to a realistic star, using the scaling relation for M_c , the critical accreted mass above which the star's magnetic moment starts to change, defined by equation (30) of Payne & Melatos (2004):

$$\frac{M_c}{M_\odot} = 6.2 \times 10^{-15} \left(\frac{a}{50}\right)^4 \left(\frac{B_*}{10^{12}\text{G}}\right)^2 \left(\frac{c_s}{10^8\text{cm s}^{-1}}\right)^{-4}. \quad (4)$$

Furthermore, we use the analytic result $\epsilon \propto a^2$ (Melatos & Payne 2005), valid for $M_a \ll M_c$, to upscale ϵ . In order to verify the fairness of this procedure, we perform runs for $a = 100$ and $a = 500$. If the curvature rescaling is fair, these runs should obey $\epsilon \propto a^2$. Computational costs limit us to achieving $M_a = 0.34 \times 10^{-4}M_\odot$. We compute ϵ , upscaled to a realistic star, for the maximum M_a for both runs, finding a relative deviation between the simulation output and the predicted scaling of $< 10^{-5}$ per cent.

3 GRAVITATIONAL WAVE STRAIN

3.1 Ellipticity

The neutron star and the piled up matter at the magnetic pole can be modelled approximately as a rigid, biaxial top, which is symmetric about the pre-accretion magnetic axis. Biaxial equilibria are of course unstable to the toroidal Parker mode and reconfigure into a triaxial equilibrium, as described in section 2.2 and Vigelius & Melatos (2008a). However, the ultimate deviations from axisymmetry are small, less than 0.1 per cent, according to Fig. 2, and can be neglected in a first analysis. In this case, we can rewrite equation (2) as $\epsilon = |I_3 - I_1|/I_1$, where I_1 and I_3 denote the moments of inertia with respect to the star's principal axes. It is important to keep in mind that we are dealing with a *prolate* spheroid, with $I_1 > I_3$; the consequences for the long-term rotational evolution are explored

in section 4.2. Frequently, authors omit taking the absolute value in the definition of ϵ resulting in a negative ellipticity for our case.

In general, the mountain axis is tilted with respect to the rotation axis. Thus the neutron star precesses freely, generating gravitational waves at f_* and $2f_*$, where $f_* = J/2\pi I_3$ is the star's spin frequency. For a biaxial star, the wave strains in orthogonal (+ and \times) polarisations can be written as (Zimmermann & Szedenits 1979; Jaranowski et al. 1998)

$$h_+(t) = \frac{1}{8}h_0 \sin 2\theta \sin 2i \cos \Phi(t) \quad (5)$$

$$+ \frac{1}{2}h_0 \sin^2 \theta (1 + \cos^2 i) \cos 2\Phi(t),$$

$$h_\times(t) = \frac{1}{4}h_0 \sin 2\theta \sin i \sin \Phi(t) \quad (6)$$

$$+ h_0 \sin^2 \theta \cos i \sin 2\Phi(t).$$

Here, θ denotes the wobble angle (between the total angular momentum \mathbf{J} and principal axis of inertia \mathbf{e}_3), i is the inclination angle (between \mathbf{J} and the line of sight, drawn from the star to the solar system barycenter), h_0 is a characteristic amplitude,

$$h_0 = \frac{16\pi^2 G}{c^4} \frac{\epsilon I f_*^2}{D}, \quad (7)$$

(where I is the moment of inertia and D is the distance to the source), and $\Phi(t)$ is the phase, including Doppler terms; for a source at rest relative to the observer, we can write $\Phi(t) = 2\pi f_* t + \Phi_0$.

Upon combining all the results in section 3, principally equation (3), Fig. 5 and the multiplication ≈ 0.6 for converting ϵ from two- to three-dimensional equilibria (section 2.1), we arrive at the following approximate formula for the ellipticity in the absence of resistivity:

$$\frac{\epsilon}{10^{-5}} = 6.82 \frac{M_a}{10^{-4}M_\odot} \left(1 + 5.5 \frac{M_a}{10^{-4}M_\odot}\right)^{-1}. \quad (8)$$

Resistive relaxation arrests the growth of the mountain (and hence ϵ) at a value of M_a , denoted M_d , which depends on \dot{M}_a (see section 2.4). Conservatively, we conclude from the results in section 2.3 that a realistic resistivity does not relax a mountain with $M_a = 1.2 \times 10^{-4}M_\odot$ over the accretion time-scale. This implies $\epsilon \leq 3.6 \times 10^{-4}$, but the true value of ϵ is expected to be much lower than the upper bound.

3.2 Signal-to-noise ratio

The signal $x(t)$ read out at the detector port is buried in noise. We assume here that the noise $n(t)$ is additive, stationary, and Gaussian, with $\langle n(t) \rangle = 0$. Then we can write (Jaranowski et al. 1998)

$$x(t) = h(t) + n(t), \quad (9)$$

where

$$h(t) = F_+(t)h_+(t) + F_\times(t)h_\times(t) \quad (10)$$

contains the beam pattern functions F_+ and F_\times , which encode the diurnal motion of the Earth.

By averaging over sky position, inclination, and polarisation, the signal-to-noise ratio can be expressed as a function of the wobble angle, h_0 , and the observation time T_0 , viz.

$$\langle d_1^2 \rangle = \frac{h_0^2 T_0 \sin^2 2\theta}{100 S_h(f_*)}, \quad (11)$$

and

$$\langle d_2^2 \rangle = \frac{4h_0^2 T_0 \sin^4 \theta}{25 S_h(2f_*)}, \quad (12)$$

assuming that the interferometer arms are perpendicular. Here, $S_h(f)$ denotes the one-sided spectral noise density of the detector.

It is sometimes desirable to average over wobble angle as well, in the absence of knowledge about a specific object. Following Payne & Melatos (2006a), we average in a manner that is unbiased towards small θ , viz. $\langle \rangle = \int_0^1 d(\cos \theta)$; cf. Thorne (1987). The final result is

$$\langle d^2 \rangle = \frac{2h_0^2 T_0}{375} \left[\frac{1}{S_h(f_*)} + \frac{16}{S_h(2f_*)} \right]. \quad (13)$$

3.3 LIGO detectability

In Fig. 6, we plot d as a function of accreted mass M_a and wobble angle θ for a standard pulsar with $f = 500$ Hz, located at a distance $D = 10$ kpc, assuming a coherent integration time of $T_0 = 14$ d. The inputs are equation (7), equation (8), equation (11), and equation (12). We neglect resistive relaxation in order to obtain an upper limit on d ; the results of section 2.3 and section 3.1 suggest Ohmic diffusion saturates d for $M_a \gtrsim 10^{-4} M_\odot$. The solid and dashed curves in Fig. 6 refer to the current and planned sensitivities of Initial and Advanced LIGO respectively, published in LIGO science requirement document and the Advanced LIGO proposal². We find that a perfectly radiating mountain with $M_a \gtrsim 10^{-4} M_\odot$ is barely detectable with Initial LIGO ($d \approx 1$) and firmly detectable with Advanced LIGO ($d \approx 10$). As M_a increases, d saturates at ~ 10 for LIGO and ~ 100 Advanced LIGO. One must remember, though, that resistive relaxation reduces these values for $M_a \gtrsim 10^{-4} M_\odot$.

An alternative way to estimate the detectability of the signal is to compare the characteristic wave strain h_0 versus the statistical threshold h_{th} . A signal is detected with a false alarm rate of 1 per cent and a false dismissal rate of 10 per cent when h_0 exceeds $h_{\text{th}} \approx 11.4 [S_h(2f_*)]^{1/2} T_0^{-1}$ (Jaranowski et al. 1998; Abbott et al. 2004). Fig. 7 displays h_0 as a function of M_a for the same pulsar as in Fig. 6. The diagonal lines give h_0 for $M_a/M_\odot = 10^{-9}, 10^{-8}, 10^{-7}, 10^{-6}, 10^{-5}, 10^{-4}, 10^{-3}$, for a biaxial (solid lines) and a triaxial (dashed lines) mountain. Also plotted as solid curves are h_{th} for Initial LIGO and Advanced LIGO for $T_0 = 14$ d, averaged over θ and i . We exclude the region $M_a \gtrsim 10^{-4} M_\odot$ (light shaded region), in which resistive relaxation prevents further growth of ϵ , and the region $2f > 1.4$ kHz (dark shaded region), because no accreting millisecond pulsars have been discovered yet in this band (they may be in the future).

Fig. 7 suggests that there is a small region $400 \lesssim$

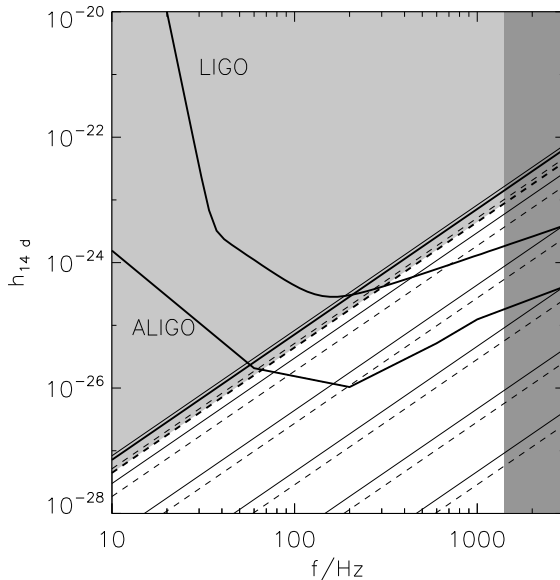


Figure 7. Amplitude h_0 of the gravitational wave signal for $M_a/M_\odot = 10^{-9}, 10^{-8}, 10^{-7}, 10^{-6}, 10^{-5}, 10^{-4}, 10^{-3}$, for axisymmetric (solid diagonal lines, bottom to top) and nonaxisymmetric (dashed lines) mountains. The sensitivities of Initial and Advanced LIGO, assuming 14 days coherent integration, are also plotted (upper and lower curves respectively). The growth of the mountain is arrested for $M_a \gtrsim 10^{-4} M_\odot$ (light shaded region) by resistive relaxation (Melatos & Payne 2005; Vigelius & Melatos 2008a). The right-hand edge is excluded at present because no accreting millisecond pulsars have been discovered with $2f_* > 1.4$ kHz (dark shaded region).

$f_*/\text{Hz} \lesssim 1400$ for which magnetic mountains are, in principle, detectable with initial LIGO. However, there are several physical mechanisms not yet considered in our modelling, most notably the sinking of the mountain into the crust, which act to reduce the gravitational wave signal. We discuss these mechanics further in section 5.

4 GRAVITATIONAL WAVE SPECTRUM

In this section, we investigate the gravitational wave spectrum in more detail. Two effects modify the spectrum away from its simplest form (delta functions at f_* and $2f_*$): global MHD oscillations, and triaxiality. We study the former without the latter in section 4.1, and vice versa in section 4.2, to isolate the physics of the two effects.

4.1 Biaxial, vibrating mountain

A magnetically confined mountain oscillates when plucked, e.g. by starquakes or fluctuations in the accretion torque (Payne & Melatos 2006a; Vigelius & Melatos 2008a). These global hydromagnetic modes appear in the gravitational wave spectrum as acoustic and Alfvénic sidebands beside the two main peaks at f_* and $2f_*$.

The top panels of Fig. 8 display the truncated Fourier transform,

² http://www.ligo.caltech.edu/advLIGO/scripts/ref_des.shtml

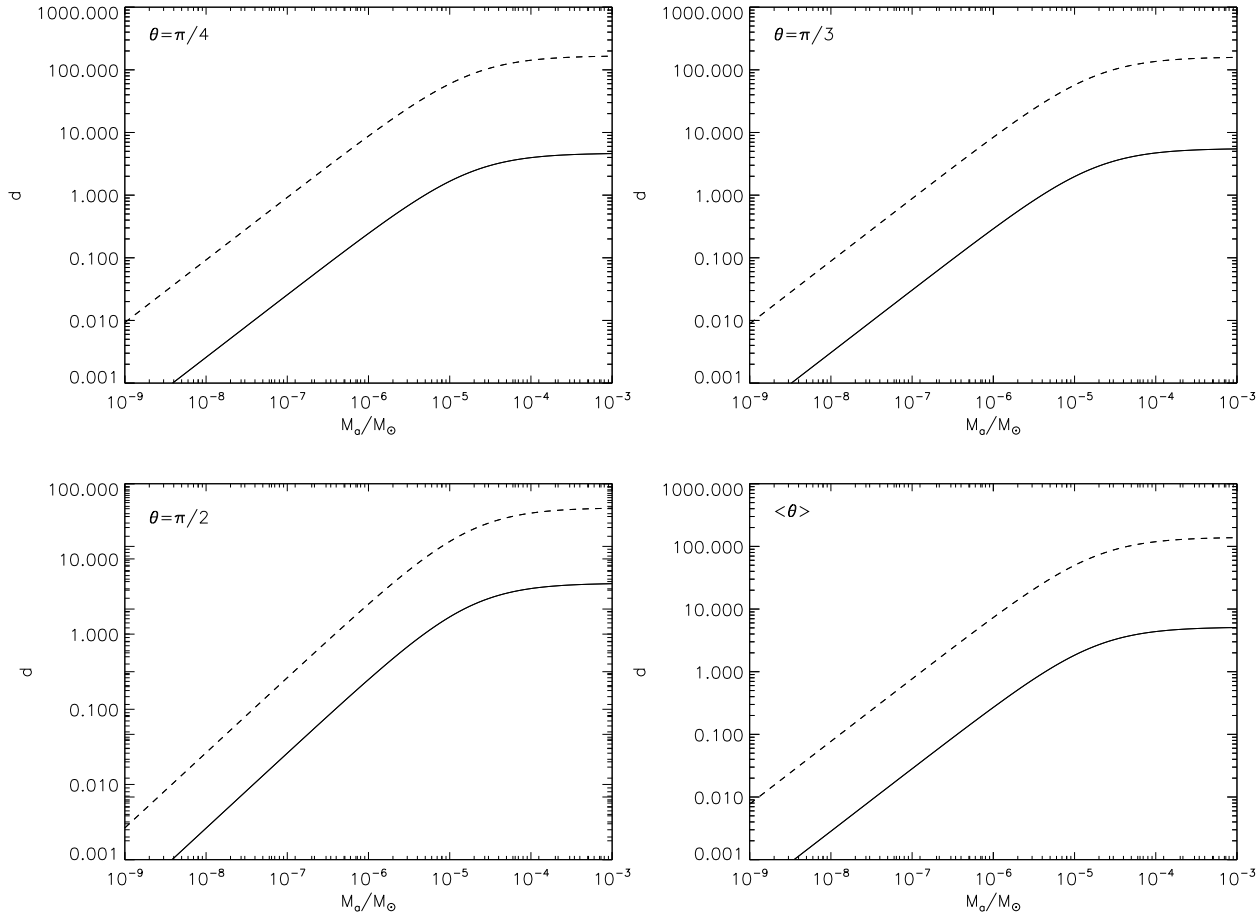


Figure 6. Signal-to-noise ratio d for $10^{-9} \leq M_a/M_\odot \leq 10^{-3}$ for the nonaxisymmetric equilibrium for Initial LIGO (solid curve) and Advanced LIGO (dashed curve) after 14 days of coherent integration. The wobble angles are: $\theta = \pi/4$ (top left), $\theta = \pi/3$ (top right), $\theta = \pi/2$ (bottom left), unbiased average over $0 \leq \theta \leq \pi/2$ (bottom right).

$$h(f) = \frac{1}{T_0} \int_0^{T_0} dt e^{i2\pi ft} h(t), \quad (14)$$

of the wave strains in the $+$ and \times polarisations, given by equations (5) and (6), for a standard star with $M_a = 1.2 \times 10^{-4} M_\odot$ at $D = 10$ kpc, with $\theta = \pi/3$ and $i = \pi/3$, assuming an integration time of $T_0 = 14$ days. For comparison, we also plot h_{th} . It is important to bear in mind that, for detection, one uses the combined signal power in both polarisations, even when the peaks in each single polarisation remain under the threshold. The wobble angle is chosen artificially large to illustrate the effect of precession. For $\theta = \pi/3$, the two peaks at f_* and $2f_*$ have similar strengths. The width of the peak, the lopsidedness, and the signal power in between are numerical artifacts caused by the discrete Fourier transform; they remain even when we input the unmodulated ϵ into equation (7). For $\theta = 0.1$, a more realistic choice [cf. PSR B1828-11, Link (2003)], the peak at $2f_*$ only reaches 28 (11) per cent of the f_* peak in the $+$ (\times) polarisation (bottom panels of Fig. 8). When the total signal power is distributed into two peaks of similar height, coincidence experiments at two frequencies become possible.

The acoustic and Alfvénic sidebands produced by the

global oscillations are very hard to see in Fig. 8, due to strong numerical damping. In a realistic neutron star, the Alfvén mode may be perpetually re-excited (e.g. by fluctuations in the accretion torque). Little is known at present about the excitation mechanism. To demonstrate the effect, however, we artificially increase the oscillation amplitude tenfold (with respect to the ZEUS-MP output) by subtracting the time average from the signal, multiplying the remaining signal by ten, and finally adding the time average again. The results appear in Fig. 9. The sidebands are clearly visible, separated by $\Delta f = 17$ Hz from the main peak. The width of the sidebands is set by the damping rate.

In principle, a high resolution spectrum of the gravitational wave signal allows us to measure M_a and the surface magnetic field from Δf (Payne & Melatos 2006a; Vigelius & Melatos 2008a). A detailed analysis of the global MHD oscillations, including the linear response to a stochastic excitation, will be attempted in a forthcoming paper.

4.2 Triaxial, nonvibrating mountain

The Parker instability experienced by an initially axisymmetric mountain saturates in a slightly nonaxisymmetric state, with $B_\phi \sim B_p$ and $Q_{12}/Q_{33} \sim 10^{-3}$, as discussed in

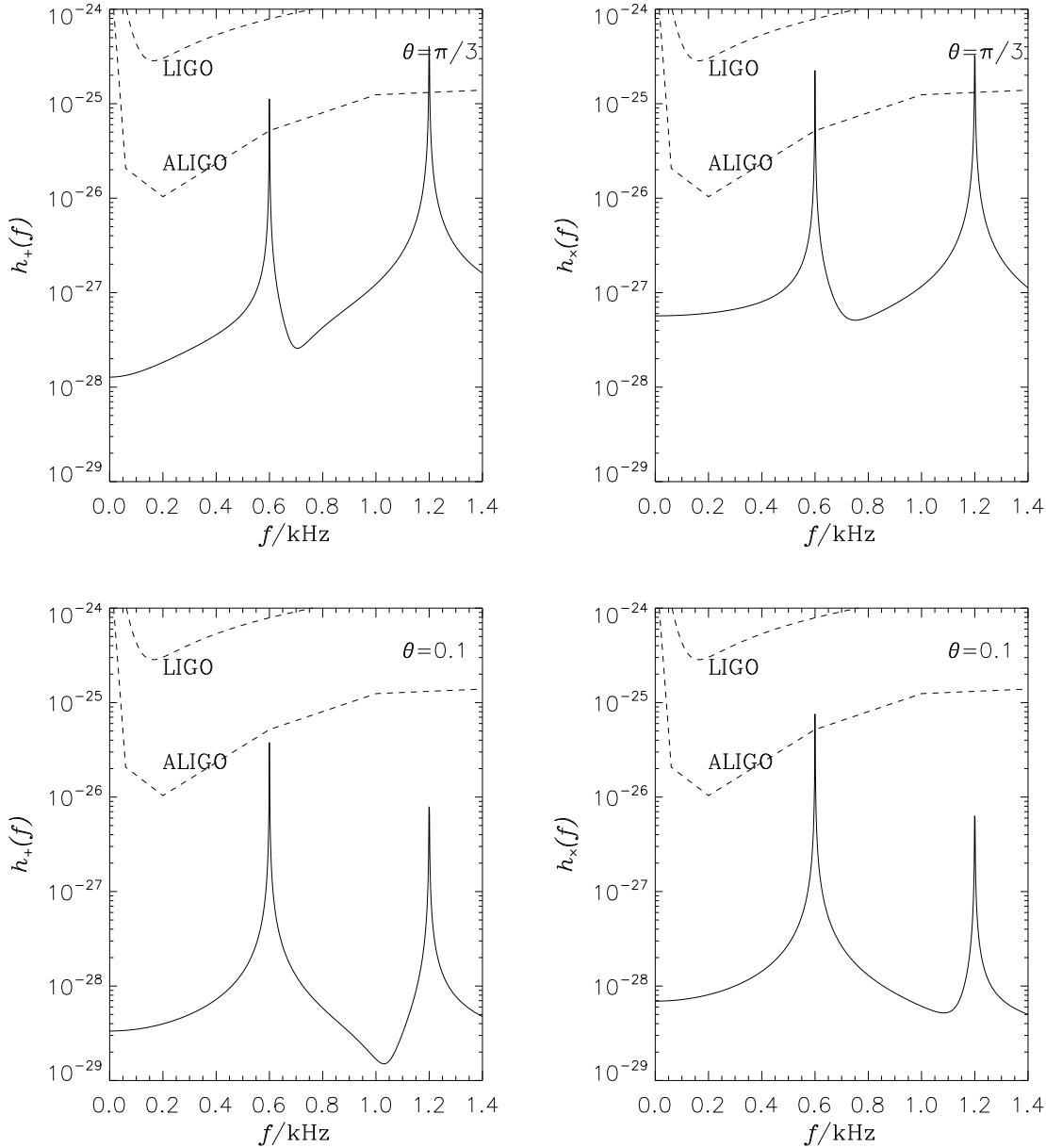


Figure 8. Fourier transform of the gravitational wave signal from a standard neutron star ($M_a = 1.4M_c$) with an axisymmetric magnetic mountain at a distance $D = 10$ kpc, with wobble angle $\theta = \pi/3$ (top panels) and $\theta = 0.1$ (bottom panels), and inclination $i = \pi/3$. The left (right) panels show the discrete Fourier transforms of the signals $h_+(t)$ [$h_\times(t)$] in the plus (cross) polarisations. The peak is not a δ function due to the finite resolution of the discrete Fourier transform. The dashed curves display the detection threshold h_{th} for Initial (upper) and Advanced (lower) LIGO, assuming an observation time of $T_0 = 14$, a false alarm rate of 1 per cent, and a false dismissal rate of 10 per cent.

see sections 2.1 and 2.2. A third, unequal principal moment of inertia introduces new features into the gravitational wave spectrum. Zimmermann (1980) computed the waveform in a small-wobble-angle expansion. Van Den Broeck (2005) extended this analysis up to second order in θ , finding

$$h_+(t) = \sum_{k=0}^1 [A_{+,k}^I \cos(\Omega_{2k}^I t) + A_{+,k}^{II} \cos(\Omega_{2k}^{II} t)] \quad (15)$$

and

$$h_\times(t) = \sum_{k=0}^1 [A_{\times,k}^I \sin(\Omega_{2k}^I t) + A_{\times,k}^{II} \sin(\Omega_{2k}^{II} t)], \quad (16)$$

with $\Omega_{2k}^I = 2\Omega_{\text{rot}} + 2k\Omega_{\text{prec}}$ and $\Omega_{2k}^{II} = \Omega_{\text{rot}} + (1 + 2k)\Omega_{\text{prec}}$, where the fundamental angular frequencies are

$$\Omega_{\text{prec}} = \frac{\pi b}{2K(m)} \left[\frac{(I_3 - I_2)(I_3 - I_1)}{I_1 I_2} \right]^{1/2} \quad (17)$$

and

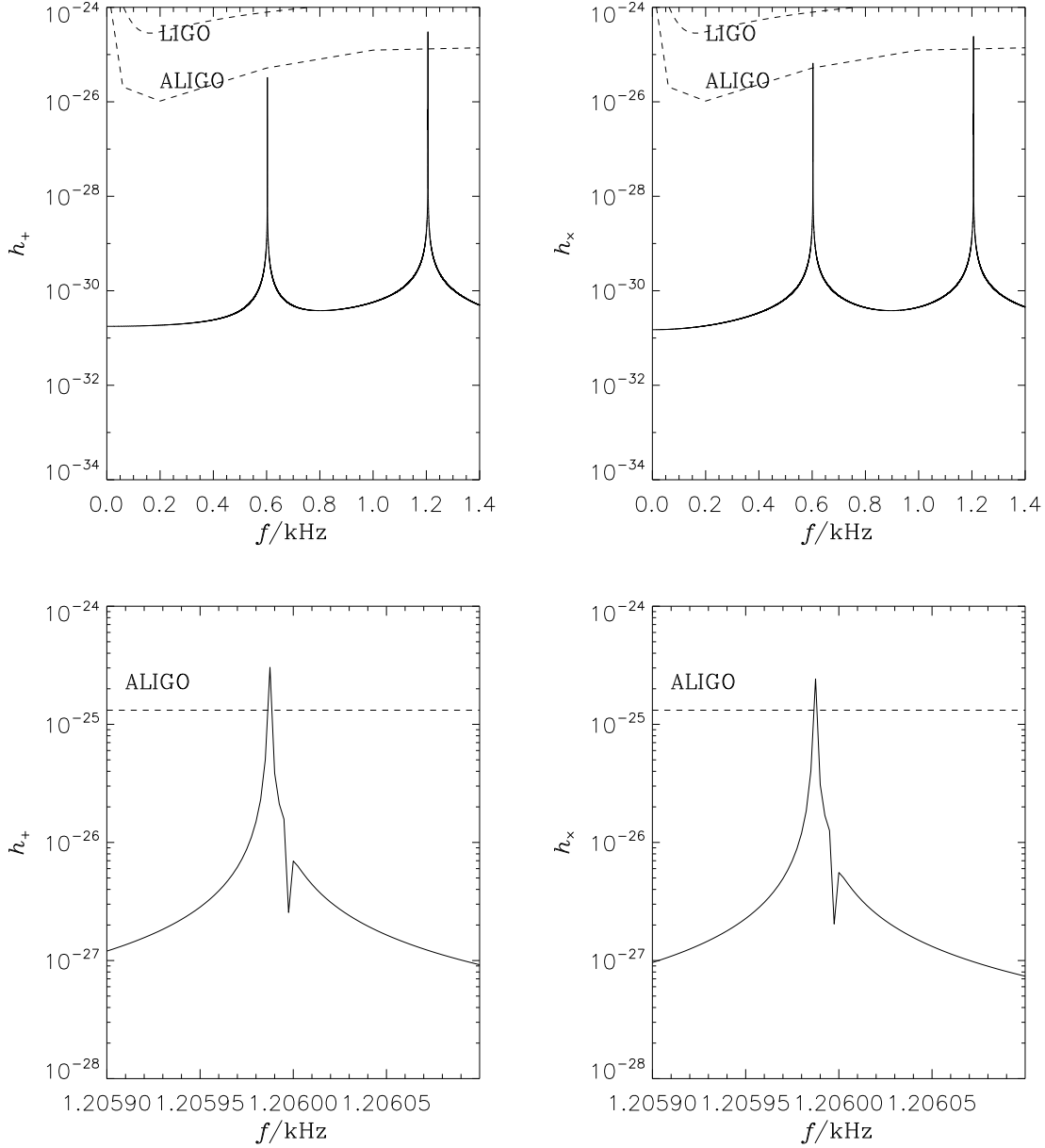


Figure 10. Fourier transform of the gravitational wave signal from a standard neutron star ($M_a = 1.4M_c$) with an nonaxisymmetric magnetic mountain at a distance $D = 10$ kpc, with wobble angle $\theta = 0.1$ and inclination $i = \pi/3$. The left (right) panels show the discrete Fourier transform of the signals $h_+(t)$ [$h_\times(t)$] in the plus and cross polarisations respectively (second order in θ). The dashed curves display h_{th} of LIGO and advanced LIGO, assuming an observation time of $T_0 = 14$ d. The lower panels zooms in on the peak at $2(\Omega_{\text{rot}} + \Omega_{\text{prec}})$, revealing the split peak due to triaxiality.

$$\Omega_{\text{rot}} = \frac{J}{I_1} - \left[1 + \frac{i}{\pi} \frac{\vartheta_4'(i\pi\alpha)}{\vartheta_4(i\pi\alpha)} \right] \Omega_{\text{prec}}. \quad (18)$$

In (17) and (18), I_1 , I_2 , and I_3 denote the principal moments of inertia, $J = (I_1^2\Omega_1^2 + I_2^2\Omega_2^2 + I_3^2\Omega_3^2)^{1/2}$ is the (conserved) total angular momentum, and $\boldsymbol{\Omega} = (\Omega_1, \Omega_2, \Omega_3)$ is the angular velocity vector. At $t = 0$, we have $\boldsymbol{\Omega} = (a, 0, b)$ without loss of generality, such that $a/b \approx \theta$ for small wobble angles. For consistency with Van Den Broeck (2005), the principal moments of inertia are ordered such that $I_1 \leq I_2 \leq I_3$ and $J^2 \geq 2EI_2$, where $2E = I_1\Omega_1^2 + I_2\Omega_2^2 + I_3\Omega_3^2$ is the (conserved) total kinetic energy. The parameter m is defined by

$$m = \frac{(I_2 - I_1)I_1a^2}{(I_3 - I_2)I_3b^2}, \quad (19)$$

$K(m)$ is the complete elliptic integral of the first kind, ϑ_4 is the fourth Jacobi theta function, with nome $q = \exp[-\pi K(1-m)/K(m)]$, and α is a solution of

$$\text{sn}[2i\alpha K(m), m] = \frac{iI_3b}{I_1a}, \quad (20)$$

where sn is the (doubly periodic) Jacobi elliptic function.

The amplitudes A_+ and A_\times for the plus and cross polarisations take the form (Van Den Broeck 2005)

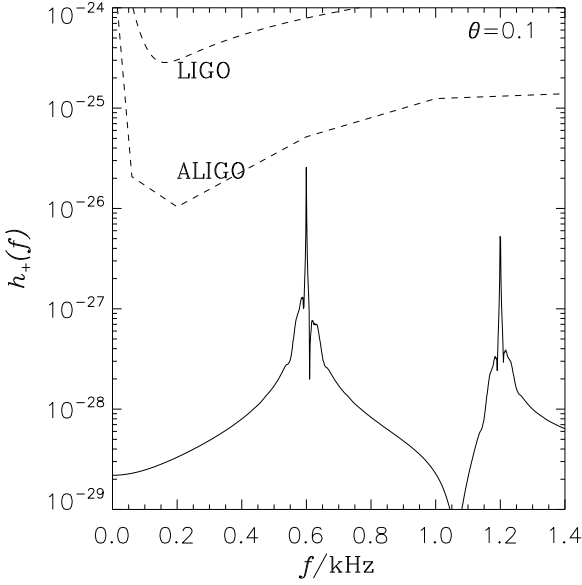


Figure 9. Fourier transform of $h_+(t)$, for a neutron star ($M_a = 1.4M_c$) at a distance $D = 10$ kpc, with wobble angle $\theta = 0.1$ and inclination $i = \pi/3$ (cf Fig. 8). The amplitude of the oscillations in ϵ has been increased artificially by a factor 10 in order to bring out the sidebands. The nonzero width of the sidebands stems from numerical damping.

$$A_{+,0}^I = -\frac{2}{D}b^2(1 + \cos^2 i)(I_2 - I_1), \quad (21)$$

$$A_{+,1}^I = \frac{2}{D}b^2[I_3 - (I_1 + I_2)/2]\gamma^2(1 + \cos^2 i), \quad (22)$$

$$A_{\times,0}^I = -\frac{4}{D}b^2(I_2 - I_1)\cos i, \quad (23)$$

$$A_{\times,1}^I = \frac{4}{D}b^2[I_3 - (I_1 + I_2)/2]\gamma^2\cos i, \quad (24)$$

$$A_{+,0}^{II} = \frac{1}{D}b^2[I_3 - (I_1 + I_2)/2]\gamma\sin(2i), \quad (25)$$

$$A_{+,1}^{II} = 0, \quad (26)$$

$$A_{\times,0}^{II} = \frac{2}{D}b^2[I_3 - (I_1 + I_2)/2]\gamma\sin i, \quad (27)$$

and finally

$$A_{\times,1}^{II} = 0. \quad (28)$$

where we omit the factor G/c^4 to avoid confusion. In (21)–(28), i denotes the inclination angle, D is the distance to the star, and $\gamma \ll 1$ is the expansion parameter

$$\gamma = \frac{I_1 a}{I_3 b}. \quad (29)$$

Equations (15) and (16) point to the existence of three distinct lines in the gravitational wave spectrum. Line I, at $2\Omega_{\text{rot}}$, stems from the departure from axisymmetry [cf. the discussion in Van Den Broeck (2005)]. A body rotating around one of its principal axes of inertia looks identical after half a period. Line II, at $\Omega_{\text{rot}} + \Omega_{\text{prec}}$, results from the free precession of a nearly axisymmetric ($I_1 \rightarrow I_2$) object in the small-wobble-angle approximation (Zimmermann 1980). Line III, appearing as a sidelobe to line I at $\Omega_0^I + 2\Omega_{\text{prec}}$,

results from the second order expansion of the precession. For a biaxial star, lines I and III coincide at the frequency $\Omega_{\text{rot}} + \Omega_{\text{prec}} = 2\pi f_*$, consistent with equation (5). Nonaxisymmetry then separates line I, which is shifted to a lower frequency and the second-order line III, which remains at $2\pi f_*$.

We compute the gravitational wave spectrum for the triaxial equilibrium (Fig. 1b) from Q_{ij} at $t = 10\tau_A$. In order to rescale Q_{ij} to a realistic curvature (see section 2.5), we employ the relation $\epsilon = Q_{33}/2I_3 \propto R_*^2$ (Melatos & Payne 2005), which implies $Q_{33} \propto M_* R_*^4$, and hence $Q_{ij} \propto M_* R_*^4$ consistent with Vigelius & Melatos (2008a)³. The (up-scaled) principal moments of inertia evaluate to $[I_1/\text{Tr}(I)] - 1 = -3.9 \times 10^{-6}$, $[I_2/\text{Tr}(I)] - 1 = -1.8 \times 10^{-6}$, and $[I_3/\text{Tr}(I)] - 1 = 5.8 \times 10^{-6}$, where $\text{Tr}(I) = 3.3 \times 10^{45}$ g cm² is the trace of the moment of inertia tensor. We also consider a star with $D = 10$ kpc, $\Omega/2\pi = 600$ Hz, and $\theta \approx a/b = 0.1$ rad. This particular choice results in $\alpha = 0.93$, $\Omega_{\text{prec}} = 0.032$ rad s⁻¹, and $\Omega_{\text{rot}} = 3.7 \times 10^3$ rad s⁻¹.

Fig. 10 depicts the spectrum (solid curves) emitted by the above star, along with h_{th} for Initial LIGO and Advanced LIGO (dashed curves), assuming an observation time of $T_0 = 14$ d. Again, all the peaks in this mock spectrum are δ functions in reality; their width stems from the finite resolution of the discrete Fourier transform. The peaks at Ω_0^I and Ω_0^{II} are clearly visible in both polarisations. Neither surpasses the noise floor unless the tunability of Advanced LIGO is exploited. A larger wobble angle improves matters. The size of θ is controlled by extraneous factors, such as the angle Ω makes with the accretion disk (Lai 2007), the accretion history, the crystallisation history of the crust (Melatos 2000; Melatos & Payne 2005), and dissipative processes in the superfluid interior (Cutler & Lindblom 1987), none of which are well understood. However, if deeply modulated, persistent X-ray pulsations emanate from a hot spot on the stellar surface at the magnetic poles, then θ must be appreciable (Chung et al. 2008).

The bottom panels of Fig. 10 zoom in on the peaks at Ω_0^{II} , revealing the second-order peak at Ω_2^{II} . We measure the amplitudes to be in the ratios $|A_{+,0}^I/A_{+,1}^I| \approx |A_{\times,0}^I/A_{\times,1}^I| \approx 25$. This shows clearly how triaxiality shifts the main peak to a lower frequency ($2\Omega_{\text{rot}}$), while only a small, second-order peak remains at $2(\Omega_{\text{rot}} + \Omega_{\text{prec}})$, as for a biaxial star. The peaks are separated by $\Delta\Omega/2\pi = \Omega_{\text{prec}}/\pi = 0.01$ Hz.

Can the extra, “triaxial” peak be exploited to facilitate detection, i.e. to increase the signal-to-noise ratio d ? The generalisation of the results of section 3.2 is straightforward, as long as we assume that the detector can resolve all three spectral lines. After averaging over sky position, inclination, and polarisation, we find

$$\langle d^2 \rangle \simeq \langle d_I^2 \rangle + \langle d_{II}^2 \rangle + \langle d_{III}^2 \rangle \quad (30)$$

with

³ By applying the same scaling to all components Q_{ij} , we effectively assume that the three-dimensional structure of the mountain scales homologously with R_* . We find empirically that this assumption holds for axisymmetric (Payne & Melatos 2004, 2007) and nonaxisymmetric configurations [see Vigelius & Melatos (2008a), and section 4.6].

$$\langle d_I^2 \rangle = \frac{16T_0 b^4}{25S_h(f_I)D^2} (I_2 - I_1)^2, \quad (31)$$

$$\langle d_{II}^2 \rangle = \frac{16T_0 b^4}{25S_h(f_{II})D^2} [I_3 - (I_1 + I_2)/2]^2 \gamma^2, \quad (32)$$

$$\langle d_{III}^2 \rangle = \frac{16T_0 b^4}{25S_h(f_{III})D^2} [I_3 - (I_1 + I_2)/2]^2 \gamma^4, \quad (33)$$

with $f_{I,II} = \Omega_0^{I,II}/(2\pi)$ and $f_{III} = \Omega_2^{II}$.

If the canonical star above ($M_a = 10^{-5} M_\odot$, $D = 10$ kpc, and $\theta = 0.1$) is observed with Initial LIGO, we expect $\langle d_I^2 \rangle = 1.6$, $\langle d_{II}^2 \rangle = 1.1$, and $\langle d_{III}^2 \rangle = 0.003$. Importantly, if one does not account for the frequency shift of line II when searching the LIGO data, one picks up only the strongly attenuated line III and hence only half of the total signal-to-noise ratio.

Once an initial detection is made, it is possible to extract the inclination, precession angle, deviation from axisymmetry, and oblateness parameter $1 - (I_1 + I_2)/2I_3$ (Van Den Broeck 2005) from the gravitational wave spectrum. Firstly, i can be found easily from the amplitude ratio of the two polarisations in any spectral line. Next, the amplitude ratio of line II and line III can (knowing i) be used to infer $I_1 a/I_3 b$. The ratio of lines I and II is proportional to $I_3 b(I_2 - I_1)/I_1 a[I_3 - (I_2 - I_1)/2]$. The line frequencies tell us Ω_{rot} and Ω_{prec} . Using the approximate relation $\Omega_{\text{prec}}/\Omega_{\text{rot}} \approx \pi[I_3 - (I_1 + I_2)/2]/2K(m)I_3$, one can finally derive the oblateness parameter $[I_3 - (I_1 + I_2)/2]/I_3$.

4.3 Precession amplitude

At present, the wobble angle θ is partly constrained by theory and observation. We know that it cannot be zero exactly, because the fluctuating magnetospheric accretion torque has nonzero components perpendicular to Ω (Lai 1999), which give $\theta \neq 0$ for finite damping. But how small is the steady-state θ ? If the magnetic axis μ is aligned with Ω , due to viscous dissipation, before the crust crystallises, then μ , Ω , and e_3 are all aligned. In this case, we see neither precession nor X-ray pulsations before accretion begins (provided the pulsations stem from a hot spot at the magnetic pole). However, a subsequently accreted mountain with a small nonaxisymmetry emits gravitational radiation at $f = 2\Omega_{\text{rot}}$ (line I), but still no X-ray radiation. On the other hand, if the crust crystallises before Ω aligns with μ , we see precession, pulsation, and gravitational radiation in all three lines (Melatos 2000; Payne & Melatos 2006a).

Gravitational-wave back-reaction damps the wobble on a time-scale $\tau \sim 10^5 \text{yr} (10^{-7}/\epsilon)^2 (\text{kHz}/f_*)^4$ (Cutler & Jones 2001), provided the star can be treated as a fluid body with an elastic crust and the precession is torque-free. On the other hand, a neutron star with an accreted mountain forms a prolate spheroid. In this case, internal dissipation increases the wobble angle ($\theta \rightarrow \pi/2$) [cf. the discussion in Cutler & Jones (2001)]. Alpar & Saulis (1988) examined the coupling of the superfluid interior and the stellar crust, finding that θ approaches $\pi/2$ over $\sim 10^4$ free precession periods.

It has been postulated that precession explains the slow variation in pulse-arrival-time residuals observed in accreting neutron stars (e.g. Her X-1) and isolated pulsars (e.g. PSR B0959-54 and PSR B1828-11) [cf. the discussion in

Akgün et al. (2006)]. Chung et al. (2008) modelled the X-ray flux modulations observed in XTE J1814-338. They found $\epsilon \leq 10^{-9}$ and $0^\circ \leq \theta \leq 5^\circ$ if the star precesses and $\epsilon \cos \theta \leq 10^{-10}$ if not. Akgün et al. (2006) modelled the radio pulses from PSR B1828-11, finding that they can be matched by a precessing, triaxial star, whose degree of nonaxisymmetry is small and whose shape is prolate. The wobble angle of this isolated pulsar is $\theta \sim 3^\circ$ (Link 2003; Stairs et al. 2000).

5 DISCUSSION

In this article, we give improved estimates for the strength and spectrum of gravitational waves from accreting millisecond pulsars. For the first time, we include the effects of non-axisymmetry and resistive relaxation on the gravitational wave signal. Furthermore, we justify the curvature down-scaling introduced in previous work (Payne & Melatos 2004, 2007; Vigelius & Melatos 2008a) and achieve self-consistent mountain configurations with $M_a \sim 10^{-3} M_\odot$, ten times larger than constructed previously, by growing them from scratch by injection. We cannot find any evidence for a growing, axisymmetric instability even at these M_a .

Taken at face value, Figs. 6 and 7 imply that mountains with $(f_*/0.3 \text{kHz})^2 (M_a/10^{-5} M_\odot) \gtrsim 1$ are detectable in principle even with Initial LIGO. With Advanced LIGO, chances are even better over the whole 0.1 – 1 kHz band for $M_a \gtrsim 10^{-6} M_\odot$. While this encouraging result was foreshadowed by Melatos & Payne (2005), this paper includes for the first time the dynamics of nonaxisymmetry and resistive relaxation, which act to weaken the signal – yet still the prospects remain bright. In principle, the noise floor of Advanced LIGO can be lowered even further by using a narrowband configuration exploiting a squeezed vacuum (Buonanno & Chen 2004), improving the sensitivity by as much as threefold for $f \lesssim 400$ Hz. A successful detection will let us test the reciprocal dependence of the gravitational wave amplitude on the magnetic dipole moment predicted for magnetic mountains by Melatos & Payne (2005).

Of course, magnetic mountains have not been detected during recent searches for low-mass X-ray binaries in the S5 LIGO data (Abbott et al. 2007; Watts et al. 2008). Moreover, for many LMXBs, the quadrupole moment predicted by Fig. 5 is too large to be consistent with the measured spin frequency, because the accretion-driven recycling process is “stalled” by the gravitational-wave spin-down torque (Bildsten 1998; Chakrabarty et al. 2003). This suggests that other physical processes exist, unaccounted for so far, which reduce the mountain. The circle of candidates has shrunk significantly since the exclusion of resistive relaxation⁴ (Vigelius & Melatos 2008b), but there are others, principally hydrodynamic sinking. In all the modelling to date, we assume that the mountain sits on a hard surface. Realistically, the neutron star crust is not impenetrable, and part of the mountain sinks into it (Konar & Bhattacharya

⁴ It is possible that the electrical resistivity is substantially higher than the contribution from electron-phonon scattering (Cumming et al. 2004) or that the Hall effect plays a dominant relaxing role (Pons & Geppert 2007). These possibilities will be pursued in future investigations.

1997; Choudhuri & Konar 2002; Payne & Melatos 2004)⁵. An attempt to treat sinking by growing mountains on top of a soft crust, modelled by a polytropic equation of state, will be presented elsewhere [Wette et al. (in preparation)]. A more sophisticated model would include the realistic, stratified nuclear composition of the crust and its evolution in response to pycnonuclear reactions (Brown & Bildsten 1998; Ushomirsky et al. 2000). The Coriolis force may also push the mountain to wander across the surface, especially in the fastest spinning LMXBs, although the enhanced magnetic field in the equatorial belt opposes the wandering (Payne & Melatos 2006b).

For simplicity, we assume an isothermal equation of state throughout this article. During the late stages of accretion ($M_a \gtrsim 10^{-3} M_\odot$), however, the magnetic mountain mass is comparable to the mass of the neutron star crust and the equilibrium exhibits a wide range of density and temperature. Pycnonuclear reactions in the deep regions ($\rho \gtrsim 10^{12} \text{ g cm}^{-3}$) feed thermal energy into an adiabatic mountain. The assumption of isothermality breaks down and a realistic equation of state for non-catalyzed matter is required (Haensel & Zdunik 1990a). In particular, the accreted material is expected to solidify at densities $\gtrsim 10^8 \text{ g cm}^{-3}$ (Haensel & Zdunik 1990b) and the crust needs to be modelled as an elastic solid (Ushomirsky et al. 2000). The effect of a realistic equation of state is subject of current work and the results will be presented elsewhere.

Finally, we note that the full (discrete and continuous) spectrum of global MHD mountain oscillations contains valuable information about the structure of the star, e.g. the strength of the surface magnetic field. In principle, this spectral information will be accessible by third-generation gravitational-wave interferometers with improved sensitivity and frequency resolution. As a first step, we will compute the continuous part of the MHD spectrum in a forthcoming paper.

REFERENCES

- Abbott B., et al., 2004, *Phys. Rev. D*, 69, 082004
 —, 2007, *Phys. Rev. D*, 76, 082001
 Akgün T., Link B., Wasserman I., 2006, *MNRAS*, 365, 653
 Alpar M. A., Saulis J. A., 1988, *ApJ*, 327, 723
 Andersson N., Kokkotas K. D., Stergioulas N., 1999, *ApJ*, 516, 307
 Bildsten L., 1998, *ApJ*, 501, L89+
 Brown E. F., Bildsten L., 1998, *ApJ*, 496, 915
 Buonanno A., Chen Y., 2004, *Phys. Rev. D*, 69, 102004
 Burderi L., Possenti A., Colpi M., di Salvo T., D’Amico N., 1999, *ApJ*, 519, 285
 Chakrabarty D., Morgan E. H., Muno M. P., Galloway D. K., Wijnands R., van der Klis M., Markwardt C. B., 2003, *Nature*, 424, 42
 Chamel N., Haensel P., 2008, *Living Reviews in Relativity*, 11
 Choudhuri A. R., Konar S., 2002, *MNRAS*, 332, 933
 Chung C. T. Y., Galloway D., Melatos A., 2008, *MNRAS* (submitted)
 Cumming A., Arras P., Zweibel E., 2004, *ApJ*, 609, 999
 Cumming A., Zweibel E., Bildsten L., 2001, *ApJ*, 557, 958
 Cutler C., 2002, *Phys. Rev. D*, 66, 084025
 Cutler C., Jones D. I., 2001, *Phys. Rev. D*, 63, 024002
 Cutler C., Lindblom L., 1987, *ApJ*, 314, 234
 Furth H. P., Killeen J., Rosenbluth M. N., 1963, *Phys. Fluids*, 16, 1054
 Haensel P., Zdunik J. L., 1990a, *A&A*, 229, 117
 —, 1990b, *A&A*, 227, 431
 Hanasz M., Otmianowska-Mazur K., Lesch H., 2002, *A&A*, 386, 347
 Haskell B., Andersson N., Jones D. I., Samuelsson L., 2007, *Physical Review Letters*, 99, 231101
 Hayes J. C., Norman M. L., Fiedler R. A., Bordner J. O., Li P. S., Clark S. E., ud-Doula A., Mac Low M.-M., 2006, *ApJS*, 165, 188
 Jahan-Miri M., 2000, *ApJ*, 532, 514
 Jaranowski P., Królak A., Schutz B. F., 1998, *Phys. Rev. D*, 58, 063001
 Jones D. I., Andersson N., 2002, *MNRAS*, 331, 203
 Jones P. B., 2004, *Physical Review Letters*, 93, 221101
 Konar S., Bhattacharya D., 1997, *MNRAS*, 284, 311
 Lai D., 1999, *ApJ*, 524, 1030
 —, 2007, preprint (astro-ph/0709.3086)
 Link B., 2003, in *Astronomical Society of the Pacific Conference Series*, Vol. 302, *Radio Pulsars*, Bailes M., Nice D. J., Thorsett S. E., eds., pp. 241–+
 Litwin C., Brown E. F., Rosner R., 2001, *ApJ*, 553, 788
 Melatos A., 2000, *MNRAS*, 313, 217
 Melatos A., Payne D. J. B., 2005, *ApJ*, 623, 1044
 Melatos A., Phinney E. S., 2001, *Publ. Astronom. Soc. Aust.*, 18, 421
 Nayyar M., Owen B. J., 2006, *Phys. Rev. D*, 73, 084001
 Owen B. J., 2006, *Classical and Quantum Gravity*, 23, 1
 Owen B. J., Lindblom L., Cutler C., Schutz B. F., Vecchio A., Andersson N., 1998, *Phys. Rev. D*, 58, 084020
 Payne D. J. B., 2005, PhD thesis, School of Physics, University of Melbourne.
 Payne D. J. B., Melatos A., 2004, *MNRAS*, 351, 569
 —, 2006a, *ApJ*, 641, 471
 —, 2006b, *ApJ*, 652, 597
 —, 2007, *MNRAS*, 376, 609
 Pons J. A., Geppert U., 2007, *ArXiv Astrophysics e-prints*
 Romani R. W., 1990, *Nature*, 347, 741
 Schatz H., Bildsten L., Cumming A., Wiescher M., 1999, *ApJ*, 524, 1014
 Shibasaki N., Murakami T., Shaham J., Nomoto K., 1989, *Nature*, 342, 656
 Stairs I. H., Lyne A. G., Shemar S. L., 2000, *Nature*, 406, 484
 Stergioulas N., 2003, *Living Reviews in Relativity*, 6, 3
 Thorne K. S., 1987, in *Three hundred years of gravitation*, Hawking S. W., Israel W., eds., Cambridge: Cambridge Univ. Press
 Ushomirsky G., Cutler C., Bildsten L., 2000, *MNRAS*, 319, 902

⁵ Zhang & Kojima (2006) took into account the contraction of the magnetosphere during magnetic burial. Ultimately, the equatorial belt is pushed into the crust when the accretion disk touches the surface of the star. In agreement with Payne (2005), one needs $M_a \gtrsim 10^{-5} M_\odot$ to significantly reduce the magnetic dipole moment. The “bottom” magnetic field set by magnetospheric contraction depends on the accretion rate.

- Van Den Broeck C., 2005, *Classical and Quantum Gravity*, 22, 1825
 Vigelius M., Melatos A., 2008a, accepted
 —, 2008b, in preparation
 Watts A., Krishnan B., Bildsten L., Schutz B., 2008, preprint (astro-ph/0803.4097), 803
 Zhang C. M., 1998, *A&A*, 330, 195
 Zhang C. M., Kojima Y., 2006, *MNRAS*, 366, 137
 Zimmermann M., 1980, *Phys. Rev. D*, 21, 891
 Zimmermann M., Szedenits Jr. E., 1979, *Phys. Rev. D*, 20, 351

APPENDIX A: GROWING MOUNTAINS WITH ZEUS-MP

In this appendix, we describe one way to grow a mountain with $M_a \gg M_c$, using the ideal-MHD code ZEUS-MP (Hayes et al. 2006) extended to include Ohmic dissipation (Vigelius & Melatos 2008b).

We start with an isothermal atmosphere (initial mass $\ll M_c$) resting on a hard surface at $r = R_*$ threaded by a dipolar magnetic field. We then inject matter quasistatically into the atmosphere from below (at $r = R_*$) along a polar subset of the magnetic field lines, imitating disk-fed accretion. We artificially boost the mass flux so as to grow the mountain in a reasonable time, albeit slowly compared to the hydromagnetic Alfvén time-scale. This is achieved by boosting the injection mass density ρ_0 while keeping the injection speed v_0 below the gravitational escape speed (i.e. escape from the simulation volume).

Mass is added at $r = R_*$ at a rate $\dot{M}(\theta) = \rho_0 v_0 \exp(-b \sin^2 \theta)$, where b is the polar cap radius scaled to R_* (Payne & Melatos 2004). By injecting at $r = R_*$ (from “below”) instead of $r = R_m$ (from “above”), we exploit the flux-freezing property of ideal MHD to avoid having to locate the changing intersection point of the flux surface $\Psi = \Psi_0$ with $r = R_m$; cf. the bootstrapping algorithm in Payne & Melatos (2007). We find empirically that a good compromise between shortening the run time while maintaining quasistatic injection is $\rho_0 = 5.1 \times 10^{10} \text{ g cm}^{-3}$ and $v_0 = 10^4 \text{ cm s}^{-1}$.

Although the magnitude of v_0 is constant, its direction must be parallel to the dipolar magnetic field everywhere at $r = R_*$, in order to respect the flux-freezing constraint. The $\theta = \pi/2$ surface is reflecting [objb.nojs(1)= 5], with normal magnetic field, which translates to $\mathbf{v}_\perp = \mathbf{B}_\parallel = 0$. The line $\theta = 0$ is also reflecting [ijb.nijs(1)= -1], with tangential magnetic field ($\mathbf{v}_\perp = \mathbf{B}_\perp = 0$). The outer r surface is outflow [cf. section 3.2 in Vigelius & Melatos (2008a)].

We first verify that the growing mountain upholds the correct mass/flux ratio. Fig. A1 displays $dM/d\psi$ for the injection simulation (squares), the Grad-Shafranov equilibrium (diamonds), and the analytic distribution $dM/d\psi = \exp(-\psi/\psi_a)$ (Payne & Melatos 2004). All match to better than one per cent. While the snapshot is taken at $t = 2\tau_A$ (which translates to $M_a = 0.46 \times 10^{-4} M_\odot$), we verify that $dM/d\psi$ remains unchanged with time.

By way of verification, we compare a grown mountain to a Grad-Shafranov equilibrium for $M_a = 1.2 \times 10^{-4}$ in Fig. A2. The left panels display the same density contours for the grown mountain (dashed curves) and the equilibrium

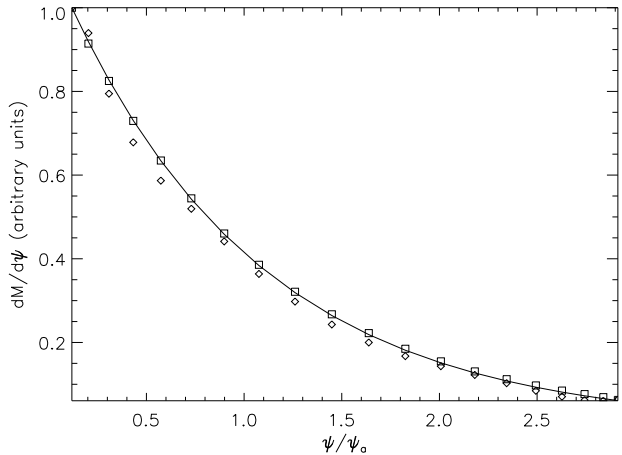


Figure A1. $dM/d\psi$ in arbitrary units as a function of ψ/ψ_a for the Grad-Shafranov equilibrium (diamonds) and the injection simulation (square). For comparison, we also include the theoretical value $dM/d\psi = \exp(-\psi/\psi_a)$ (solid curve). The snapshot is taken at $t = 2\tau_A$, although the mass-flux ratio remains constant with time, of course.

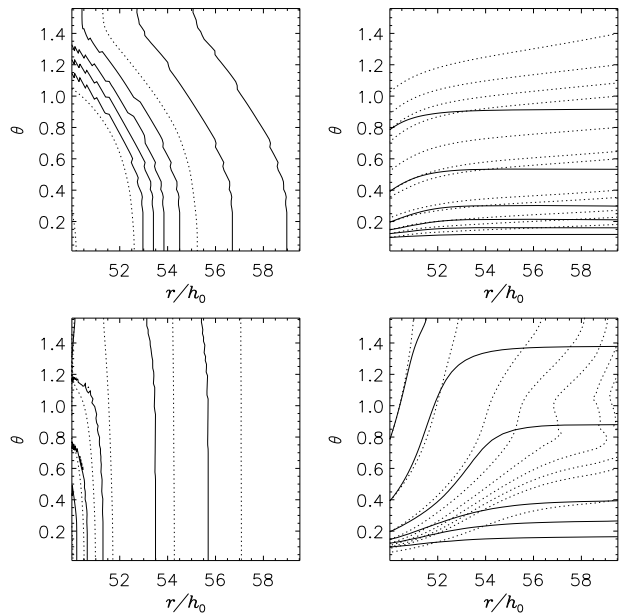


Figure A2. Meridional section of density contours (left) and magnetic field lines (right) for a grown mountain (dashed curve) and a Grad-Shafranov equilibrium (solid curve) with $M_a = 0.1M_c$ (upper panels) and $M_a = M_c$ (lower panels). While the agreement in the density is good, discrepancies in the magnetic field arise due to the different boundary conditions at $r = R_m$ (see text).

(solid curves), for $M_a = 0.1M_c$ (top panels) and $M_a = M_c$ (bottom panels). The density contours in the region close to $0 \leq \tilde{x} = (r - R_*)/h_0 \leq 2$ match reasonably well, with a deviation of less than one per cent radially and five per cent laterally. While the magnetic field lines match close to the stellar surface, there is a considerable discrepancy in the (less important) outer regions, where B is weak (and indeed ρ is small). This stems from the different implementation

of the outer boundary condition at $r = R_m$. The **outflow** boundary condition in ZEUS-MP enforces a vanishing gradient of \mathbf{B} at $r = R_m$, while Payne & Melatos (2004) enforce $\partial\psi/\partial r = 0$, thereby imposing the additional constraint $B_\theta = 0$. The exact form of the outer boundary condition depends on the interaction of the magnetosphere with the accretion disk and is poorly known. We are not concerned with the details and just note that the magnetic field decays $\propto r^{-3}$, such that it is several orders of magnitude lower than at the surface.